Energy Storage Materials 46 (2022) 563–569

Contents lists available at ScienceDirect

Energy Storage Materials

journal homepage: www.elsevier.com/locate/ensm

Stabilized Li metal anode with robust C-Li_3N interphase for high energy density batteries

Mintao Wan[a], Xiangrui Duan[a], Hao Cui[b], Junmou Du[a], Lin Fu[a], Zihe Chen[a], Zhao Lu[c], Guocheng Li[a], Yuanjian Li[a], Eryang Mao[a], Li Wang[b,*], Yongming Sun[a,*]

[a] Wuhan National Laboratory for Optoelectronics (WNLO), Huazhong University of Science and Technology (HUST), Wuhan, China
[b] Institute of Nuclear & New Energy Technology, Tsinghua University, Beijing 100084, China
[c] Huazhong University of Science and Technology Analytical & Testing Center, China

ARTICLE INFO

Keywords:
Lithium metal composite anode
Interphase
Electrochemical cycling
Electrochemo-mechanical stability
Energy density

ABSTRACT

The combination of commercial high-voltage cathode and a thin lithium metal anode has emerged as a promising approach to realize rechargeable high energy density lithium batteries. However, abundant challenges, including huge volume change of Li metal and its severe side reactions with electrolyte for wide electrochemical potential window, hamper the practical application of lithium metal anode in high energy density batteries. In this work, we reported a Li/graphene composite electrode with in situ formed robust C/Li_3N interphase (Li/graphene-C/Li_3N electrode). Stabilized by the graphene framework, the electrode can endure large volume change during lithium stripping/plating cycles and realize stable cycling. The Li_3N protection layer can not only help the composite electrode to avoid the direct physical contact between active metallic lithium and electrolyte, and suppress the side reactions between them, but also help to homogenize Li^+ diffusion and plating/stripping behaviors due to its high ionic conductivity. As a result, the composite structure and electrochemical interphase stability enable superior electrochemical performance of the Li/graphene-C/Li_3N electrodes. As a demonstration, the Li/graphene-C/Li_3N symmetric cell displayed a low and stable overpotential for more than 1000 hours at 1 mA cm^{-2} and 1 mAh cm^{-2}. $LCoO_2$||Li/graphene-C/Li_3N cell delivered a high energy density of 694.05 Wh kg^{-1} in the working potential range between 2.8 V and 4.6V and displayed high Coulombic efficiency of over 99% for more than 150 cycles, showing promising for practical high energy density lithium metal batteries.

1. Introduction

Lithium ion batteries have dominated the portable electronics such as cellphones and laptops, and they are the power sources of electric vehicles that are penetrating into the transport industry [1–5]. Nevertheless, the energy density of current lithium battery systems using graphite anode and layered oxide or phosphate cathode (e.g., $LiCoO_2$, $LiNi_{0.6}Co_{0.2}Mn_{0.2}O_2$, and $LiFePO_4$, etc) cathode is approaching their bottleneck and could not meet the increasing energy density requirements of the above applications [6,7]. Among high energy density lithium battery systems (e.g., Li-S batteries, Li-air batteries, and high-voltage Li metal batteries, etc) [8–11], high-voltage lithium metal batteries using lithium metal anodes and high-voltage cathodes are promising candidates and have the potential to be successful for the short term. High-voltage cathode materials, such as $LiCoO_2$ (LCO), $LiNi_{0.5}Mn_{1.5}O_4$ (LNMO) and $LiNi_xCo_yMn_{1-x-y}O_2$ (NCM) cathode, can deliver higher energy density due to the extended working potential at high voltage region, and increased capacity in comparison to that in current batteries, and have already made tremendous progress [12–14]. Also, electrolytes for these high-voltage cathodes have received extensive research progresses, which ensures the stable electrochemical performance of cathodes at elevated voltage [15–18]. Lithium metal anode delivers highest theoretical specific capacity (3860 mAh g^{-1}) and lowest potential (−3.040 V *vs.* standard hydrogen electrode), which are beneficial for realizing high energy density batteries [19,20]. Nevertheless, Li metal anode is still premature for practical application, especially for high-voltage batteries. Its encounters high chemical reactivity with electrolyte, uneven Li metal plating/stripping behavior and large volume change during Li metal stripping/plating process, leading to poor practical electrochemical performance and even safety concerns [10,21,22]. The electrochemical performance of thin Li metal electrode that is preferred for high energy density of Li metal batteries is even inferior than its thick counterpart, since mechanical pulverization of the electrode and active Li exhaustion occurs within very limited cycle number [23–25].

---

* Corresponding authors.
E-mail addresses: wang-l@tsinghua.edu.cn (L. Wang), yongmingsun@hust.edu.cn (Y. Sun).

https://doi.org/10.1016/j.ensm.2022.01.044
Received 29 October 2021; Received in revised form 5 January 2022; Accepted 21 January 2022

To make lithium metal anode viable, numerous research efforts have been dedicated to stabilizing the interface between lithium metal and the electrolyte, including electrolyte engineering [26–29], building artificial protection layer for lithium metal [30–32], and designing of three-dimension (3D) host for the lithium metal [33–38]. Despite of these great progresses in stabilizing Li metal, they often cannot resolve all the issues that Li metal anode faces. These approaches often only solved the electrochemical instability or the mechanical instability of the electrode-electrolyte interface. For example, filling Li metal into a 3D host enhances the mechanical stability of Li metal, and reduces the overall volume change of the electrode. However, the issue of side reactions between the electrolyte and active Li has not been addressed. On the other hand, the construction of lithium metal using artificial interface or electrolyte engineering could solve the interphase instability of metallic Li, but these electrodes could not stabilize the overall structure due to the large volume change during the plating/stripping cycling. The fluctuation of electrode-electrolyte interface caused by the volume change would destroy the preformed interphase structure and deteriorate the electrochemical performance. Therefore, it is desirable to develop an approach to address mechanical stability and interphase stability simultaneously and realize high-performance Li metal anode.

In this work, we in situ introduced a robust C-Li_3N interphase of Li/graphene composite electrode, which realized both good electrochemical interphase stability and mechanical stability. The stable C-Li_3N protection layer on the top of Li/graphene composite isolated the active metallic lithium from the electrolyte, suppressed the side reactions between metallic lithium and electrolyte, and prevented continuous active lithium consumption during battery cycling. In addition, the ionic conductive Li_3N interphase structure enabled fast and homogeneous Li^+ diffusion and thus uniform Li plating/striping behavior, and the graphene host minimized the overall volume change of the composite lithium metal anode. As a result, the Li/graphene-C/Li_3N anode exhibited superior electrochemical stability during electrochemical lithium stripping/plating processes and enabled a long-life and high energy density of the LCO||Li/graphene-C/Li_3N batteries with wide operational range of 2.8 – 4.6 V.

2. Results and discussion

2.1. Fabrication and characterizations of Li/graphene-C/Li_3N electrode

Li/graphene-C/Li_3N electrode was achieved by infusing molten lithium into the C_3N_4/graphene oxide composite film in an Ar-filled glove-box (Fig. 1a). G-C_3N_4 nanosheets was fabricated through a simple thermal polycondensation method. The X-ray diffraction (XRD) pattern of the g-C_3N_4 nanosheets showed a broad peak at 27.2°, which could be assigned to the (002) crystal plane of g-C_3N_4 (Figure S1) [39]. Transmission Electron Microscopy (TEM) images revealed that these g-C_3N_4 nanosheets were several micrometers in length and several nanometers in thickness, and they showed a laminar morphology similar to graphene (Figure S1). Composite film consisting of graphene oxide and g-C_3N_4 was fabricated as framework for Li/graphene-C/Li_3N, which was fabricated through a vacuum filtration process. During the operation, g-C_3N_4 suspension was first added, followed by graphene oxide suspension. As a result, g-C_3N_4 would stay on the top of the C_3N_4/graphene oxide composite film. Due to the layer structure of both C_3N_4 and graphene oxide, they showed good mechanical adhesion with each other and formed a compact structure. when the C_3N_4/graphene oxide film was placed in contact with the molten lithium under 300 °C, molten lithium infused into it spontaneously due to the capillary force of the pore structure between the layers of C_3N_4/graphene oxide film and the chemical affinity between them [40]. Moreover, during the infusion process, the molten lithium metal reacted with g-C_3N_4 to produce Li_3N [$12Li+C_3N_4 \rightarrow 4Li_3N+3C$], and form a C-$Li_3N$ surface layer of the Li/graphene-C/Li_3N composite electrode (Fig. 1a).

Diffraction peaks at 22.93° and 46.83°, for alpha-Li_3N were observed in the XRD pattern of Li/graphene-C/Li_3N composite electrode, verifying the formation of Li_3N during the lithium infusion process (Fig. 1b). The signals for C_3N_4 disappeared, suggesting that the g-C_3N_4 was converted into Li_3N and carbon. It is noted that crystalline Li_3N was not observed when C_3N_4 was directly used as the host for electrochemical Li plating [41], highlighting the importance of using molten lithium to enable the conversion from g-C_3N_4 to crystalline Li_3N with high ionic conductivity. X-ray photoelectron spectroscopy (XPS) analyses were performed to reveal the surface electronic state of the elemental composition. The high-resolution Li1s and N1s spectra showed peaks at 55.3 eV and 398.6 eV, respectively, confirming the existence of Li_3N on the surface the Li/graphene-C/Li_3N composite (Fig. 1c) [41,42]. In addition, there was no signal of metallic lithium in the high-resolution Li1s spectrum, which suggested that the entire electrode was completely covered by the Li_3N surface protection layer (Fig. 1c). The high ionic conductivity of Li_3N was expected to efficiently homogenize the Li^+ ion flow and enhance its transportation across the electrode surface, and lead to a uniform lithium plating and stripping behavior [43,44]. Besides, the Li_3N protection layer could work as physical shielding, avoid the direct contact between active Li and electrolyte, thus minimizing the side reactions and improving the electrochemical cycling stability.

Scanning electron microscopy (SEM) investigation was further performed to investigate the morphology and structure of the Li/graphene-C/Li_3N composite electrode. The cross-section SEM image of the Li/graphene-C/Li_3N composite electrode indicated that gaps between the C_3N_4 and graphene oxide nanosheets were filled by metallic Li uniformly from the top surface to the bottom, indicating the uniform lithium implantation of the graphene oxide/C_3N_4 framework (Fig. S4 and Fig. 1d). Such framework could act as a stable host for metallic Li, and buffer the volume change during the electrochemical Li plating and stripping process, which supports the formation of stable SEI on the electrode surface [40]. The results of cross-section SEM images coupled with energy dispersive X-ray (EDX) elemental mapping images of Li/graphene-C/Li_3N electrode indicated that nitrogen element was uniformly and densely dispersed on the surface of the electrode, supporting the formation of dense Li_3N protection layer on the top of the Li/graphene-C/Li_3Ncomposite electrode (Fig. 1e). This novel structure, which combined the advantages of both interphase protection layer with good ionic conductivity and a stable 3D lithiophilic framework, could simultaneously guarantee the electrochemical and mechanical stability of lithium metal electrode and showed promise for the application in high-performance lithium metal batteries.

2.2. Electrochemical stability of Li/graphene-C/Li_3N electrode

The composition and structure of interphases play a crucial role for the electrochemical performance of Li metal anode. The uniform Li_3N surface layer of the Li/graphene-C/Li_3N anode not only can isolate the active lithium from corrosive electrolyte and inhibit its decomposition, but also can homogenize Li^+ flux and enable stable lithium plating/stripping behavior, thus enabling a stable electrode structure. In consideration of its pairing with high-voltage cathode for high energy density batteries, 4M lithium bis(fluorosulfonyl)imide (LiFIS) in dimethyl carbonate (DMC) was used as electrolyte, which possessed broad electrochemical window in comparison to regular commercial carbonate electrolyte [45]. During cycling, the component of electrolyte took part in the formation of SEI, which decided the interphase property of anodes. High-resolution F 1s and S 2p XPS spectra with different Ar sputtering times were collected to reveal the surface SEI ingredients of the lithium metal electrode and Li/graphene-C/Li_3N electrode after 5 lithium stripping/plating cycles. Fig. 2a and 2b compared the chemical environment of F and S elements derived from the electrolyte after Ar sputtering for different times. After 1 minute's Ar sputtering, the Li/graphene-C/Li_3N electrode exhibited high intensity of LiF (684.93 eV in F 1s) signal in the high-resolution F1s spectrum (Fig. 2a left), sulfate

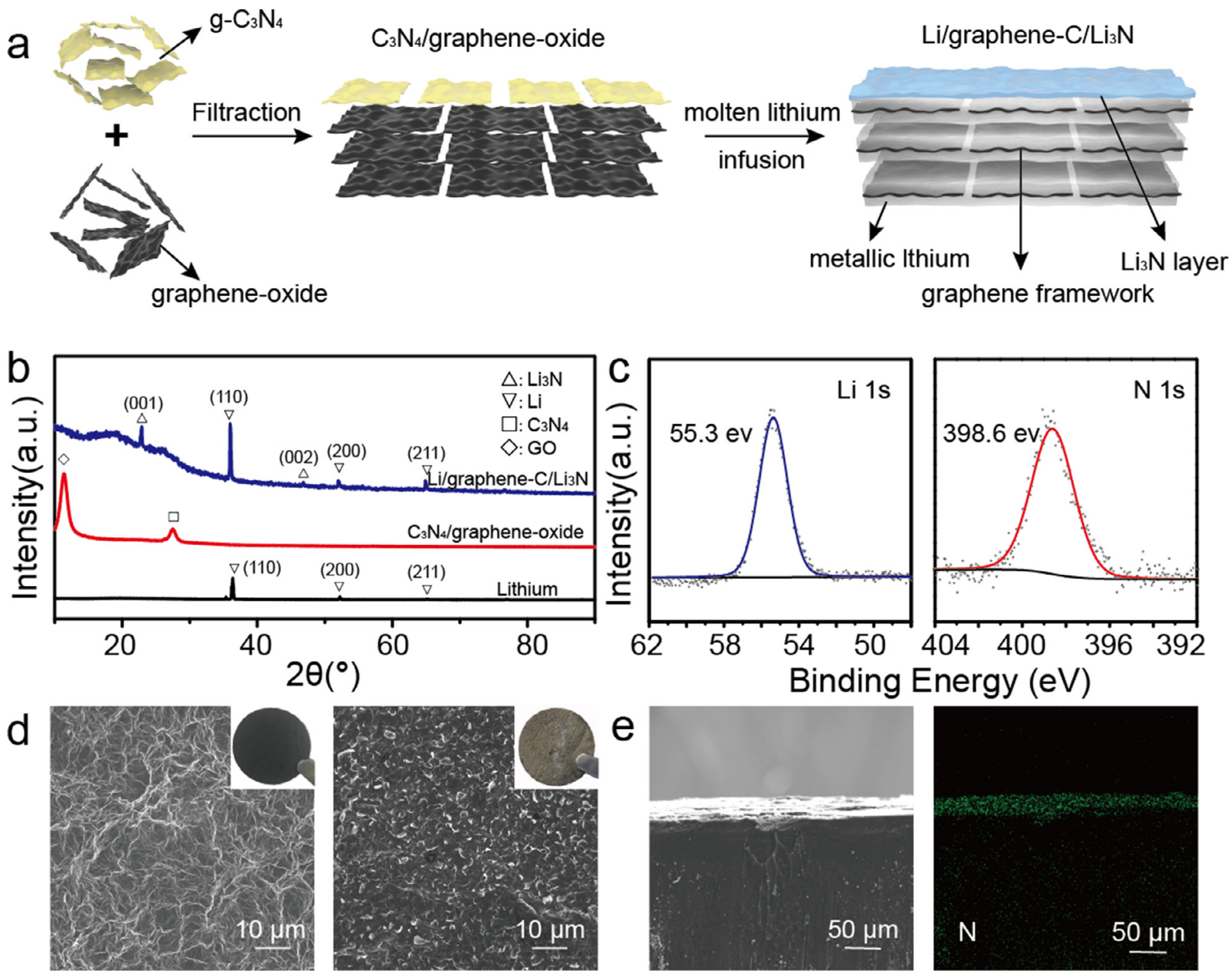

Fig. 1. Fabrication and characterizations of the Li/graphene-C/Li_3N composite electrode. a, Schematic of the fabrication of the Li/graphene-C/Li_3N composite electrode. b, X-ray diffraction patterns of the lithium metal foil, C_3N_4/graphene film, and the as-fabricated Li/graphene-C/Li_3N composite electrode. c, High-resolution Li 1s and N 1s X-ray photoelectron spectroscopy spectra for the Li/graphene-C/Li_3N electrode after surface cleaning by Ar^+ sputtering. d, Top-view SEM image of the C_3N_4/graphene film (left) and Li/graphene-C/Li_3N composite electrode (right). e, cross-section SEM image of the Li/graphene-C/Li_3N composite electrode and the corresponding EDX elemental mapping image for N.

(170.88 eV/169.70 e V in S 2p) and polythionate (168.58 eV/167.40 eV in S 2p) signals in the high-resolution S2p spectrum (Fig. 2b left), respectively, revealing the reaction between the electrode and electrolyte, and the formation of LiF and sulfate containing SEI. It is noted that the intensity of element S and F signals significantly decreased with increasing sputtering time from 1 to 20 min, and remained a very low relative value with increasing sputtering time to 40 min. The significantly decreased intensity of LiF and sulfate signals indicated that dense Li_3N layer of the Li/graphene-C/Li_3N electrode isolated the FSI^- in electrolyte from reactive metallic lithium, and enabled the formation of thin and stable SEI on the Li/graphene-C/Li_3N electrode surface. The appearance of S-F bond (687.69 eV in F 1s and 173.13 eV/171.95 eV in S 2p) and S-N bond (163.90 eV/162.72 eV in S 2p) indicated the existence of free FSI^- in the SEI [46]. FSI^- remained stable and did not continuously decompose after the formation of stable SEI on the Li/graphene-C/Li_3N electrode (Fig. 2a mid, right and Fig. 2b mid, right). Different from that of the Li/graphene-C/Li_3N electrode, S element in the pure lithium metal electrode after cycling existed mainly in the form of polysulfide (161.70 eV/160.52 eV in S 2p), polythionate, and sulfate (Fig. 2a mid, right and Fig. 2b mid, right). The strong peaks for LiF in the high-resolution F1s XPS spectrum and polysulfides in the high-resolution S2p XPS spectrum were observed after 40 minutes' Ar sputtering, which suggested that FSI^- of the electrolyte continuously reacted with the metallic Li to produce LiF and polysulfide and thus the continuous corrosive reactions of metallic Li. In addition, high intensity for S-F bond and negligible intensity for S-N bond were observed in the high-resolution S2p spectra for the pure lithium metal electrode, further proving the continuous decomposition of the FSI^- on the electrode surface during the operation of battery (Fig. 2b left). The constant side reactions between metallic Li and electrolyte would lead to a rapid depletion of the electrolyte and active lithium, and shorten the battery life.

The uneven Li stripping/plating behavior with relatively infinite volume change would lead to the repeated fracture and re-growth of SEI during electrochemical cycling, which continuously consume electrolyte and active lithium. Therefore, realization of uniform Li stripping/plating behavior and a mechanically stable structure is of vital importance for a practical lithium metal electrode. In order to reveal mechanical stability of the Li/graphene-C/Li_3N composite electrode, SEM and EDX characterizations were performed before and after cycling. Fig. 3a and b compared top-view SEM images of the Li/graphene-C/Li_3N electrode and pure Li metal electrode at different stripping and plating states. A huge and deep cavity with size of >85 μm was observed on the surface of Li metal after electrochemical Li stripping (Fig. 3a left). In contrast, smooth surface with negligible pinholes was observed for the

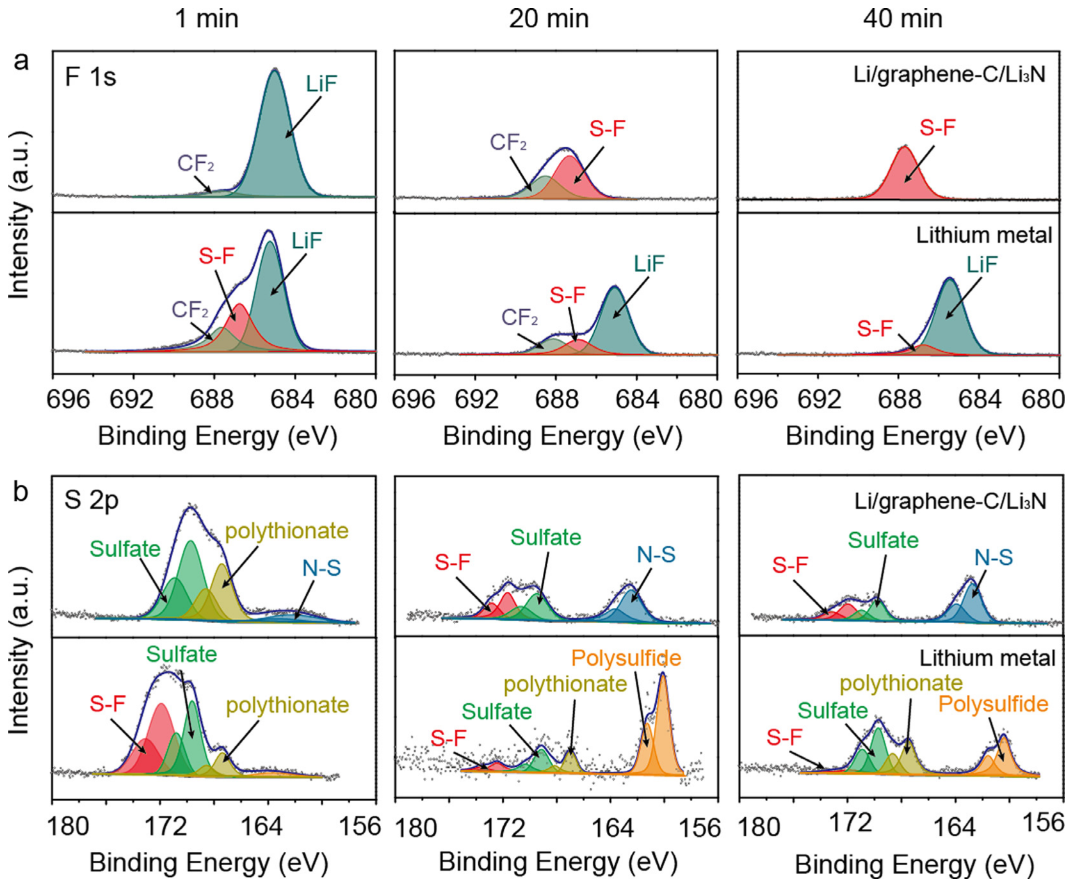

Fig. 2. High-resolution (a) F 1s and (b) S 2p XPS spectra for lithium metal electrode and Li/graphene-C/Li_3N electrode after 5 cycles in electrolyte of 4 M LiFSI in DMC after Ar^+ sputtering for different times.

Li/graphene-C/Li_3N electrode under the same test conditions, indicating its uniform and stable lithium stripping behavior. (Fig. 3b left). These results indicated that the ionically conductive Li_3N protection layer was beneficial for homogenizing Li^+ flux during the electrochemical stripping process. Also, no lithium dendrites were observed on the surface of the Li/graphene-C/Li_3N electrode after the following Li plating (Fig. 3b middle, Fig. S5 b). In contrast, a large number of lithium dendrites were observed on the surface of lithium metal electrode after Li plating (Fig. 3a middle, Fig. S5 b), which further led to the formation of a porous and brittle interphase layer after repeated Li stripping/plating cycles (Fig. 3a middle and right). The thickness of this porous interphase layer reached ~59 μm after 50 stripping/plating cycles at 1 mAh cm^{-2} and 1 mA cm^{-2}, as revealed by the results of cross-section SEM images (Fig. 3e). High-intensity signals of S, O, and F elements were observed in this porous interphase layer in the EDX element mapping images, indicating the puncture of electrolyte into this porous interphase layer and supporting the continuous side reactions between electrolyte (Fig. 3e). In contrast, the surface of the Li/graphene-C/Li_3N electrode remained compact and flat after 50 Li plating/stripping cycles (Fig. 3b right). The signals of S, O, and F elements were only observed on the surface layer of the Li/graphene-C/Li_3N electrode in the cross-section SEM image and EDX element mapping images, again supporting the dense Li deposition behavior and significantly suppressed side reactions due to the introduction of protective Li_3N surface layer and robust 3D graphene framework (Fig. 3f).

To investigate the electrochemical stability of the Li/graphene-C/Li_3N electrode, electrochemical impedance spectroscopy (EIS) measurements were also carried out. Figs. 3c and 4d compared the Nyquist plots of Li||Li and Li/graphene-C/Li_3N||Li/graphene-C/Li_3N symmetric cells after different lithium stripping/plating cycles at 1 mA cm^{-2} and 1 mAh cm^{-2}. The pristine pure Li electrode showed a much higher interfacial resistance of more than 200 ohms before cycling (Fig. 3b). Then the interfacial resistance of the pure Li electrode decreased to ~ 60 ohms after the first cycle due to the formation of dendritic lithium deposits with increased surface area. In contrast, the Li/graphene-C/Li_3N electrode showed a small initial interfacial resistance of ~15 ohm and decreased to ~5 ohms after the first cycle (Fig. 3d). The much smaller interfacial resistance of pristine Li/graphene-C/Li_3N electrode and its good stability after cycling suggested its high interphase ionic conductivity and good electrochemical stability. Warburg factor (σ) of the cells was calculated based on the corresponding Z_{re} *vs.* $\omega^{-1/2}$ plots after the first cycle ('Z_{re}' is the real part of Nyquist impedance, 'ω' is frequency in the electrochemical impedance spectroscopy test, and 'σ' is the slope of the straight line in Fig. S6). The Warburg factor (σ) of Li/graphene-C/Li_3N||Li/graphene-C/Li_3N symmetric cell (σ_1) and Li||Li symmetric cell (σ_2) were 5.622 and 38.738, respectively. The apparent diffusion coefficient of lithium ions for the Li/graphene-C/Li_3N electrode was almost fifty times higher than that of the bare Lithium metal electrode according to the equation [47]:

$$D = R^2T^2/2A^2n^4F^4C^2\sigma^2$$

where R is the gas constant, T is the room absolute temperature in experiment, A is the surface area of the electrode, n is the number of electrons per molecule attending the electronic transfer reaction, F is Faraday constant, C is the concentration of lithium ions. The much higher lithium ion diffusion coefficient of the Li/graphene-C/Li_3N electrode could be attributed to ion-conductive Li_3N interphase layer that accelerated the Li^+ transportation, homogenized the metallic Li plating, and upgraded

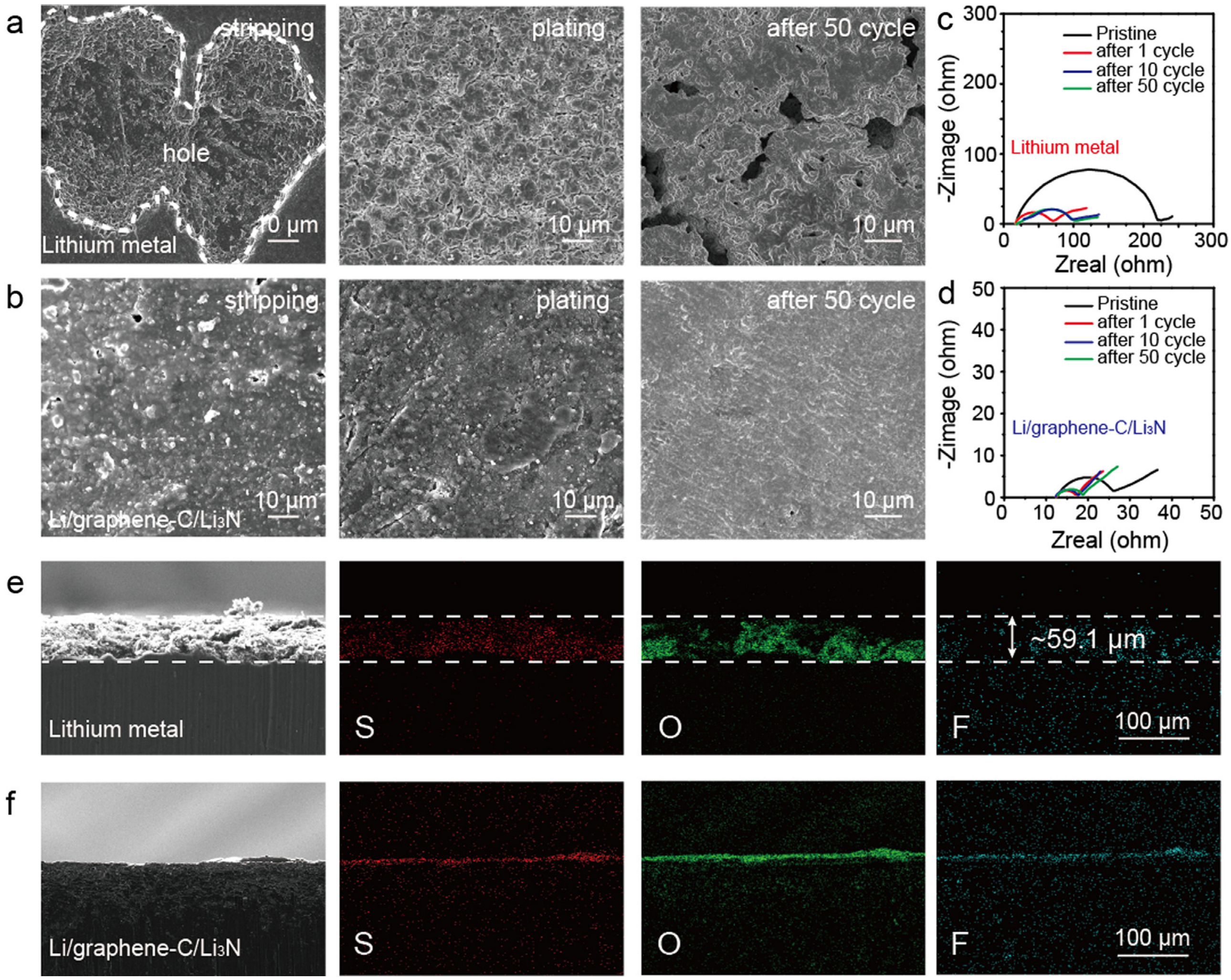

Fig. 3. SEM and EIS investigation of lithium metal electrode and Li/graphene-C/Li_3N electrode. (a, b) Top-view SEM images of lithium metal electrode and Li/graphene-C/Li_3N electrode after lithium stripping (left), a full lithium stripping/plating cycle (middle), and 50 lithium stripping/plating cycles (right) at 1 mAh cm^{-2} and 1 mA cm^{-2} (scale bar, 10 μm). (c, d) Nyquist plots of Li||Li (c) and Li/graphene-C/Li_3N||Li/graphene-C/Li_3N symmetric cells (d) after different lithium stripping/plating cycles under 1 mA cm^{-2} and 1 mAh cm^{-2}. (e, f) Cross-sectional SEM images and the corresponding EDX mapping images of a lithium metal electrode (f) and a Li/graphene-C/Li_3N electrode (g) after 50 stripping/plating cycles at 1 mAh cm^{-2} and 1 mA cm^{-2}.

its electrochemo-mechanical stability. The interfacial resistance of pure Li electrode increased to ~80 ohms after 50 cycles, indicating its continuous electrochemical degradation. The interfacial resistance of the Li/graphene-C/Li_3N electrode remain small and stable, and the value was only ~6 ohms after 50 cycles, similar to the value after the 1st cycle, verifying the good stability of the Li/Li_3N/graphene electrode.

The superior electrochemical and mechanical stability of Li/graphene-C/Li_3N electrode could be ascribed to the synergistic effect of ironically conductive Li_3N interphase layer and robust graphene framework. The dense Li_3N protection layer on the electrode surface could homogenous the lithium-ion flux, and the high ionic conductivity and electronic resistivity of Li_3N could compel the lithium ions to come cross the Li_3N protective surface layer and produce uniform Li deposition layer below. In addition, the graphene framework could act as a stable host for the metallic lithium, which reduced the volume change of the entire electrode and ensured stable electrode-electrolyte interphase as well as a stable SEI. In contrast, continuous movement of electrode-electrolyte interphase and uneven Li plating/stripping behaviors for bare Li metal electrode took place for bare metallic Li electrode, leading to repeated break and repair of SEI, continuous consumption of electrolyte, and increase in electrode resistance.

2.3. *Electrochemical performance of Li/graphene-C/Li_3N anode*

The electrochemical performance of Li/graphene-C/Li_3N||Li/graphene-C/Li_3N symmetric cell and $LiCoO_2$||Li/graphene-C/Li_3N cell was investigated with 4M LiFSI in DMC as electrolyte. Fig. 5a compared the voltage profiles for the Li||Li symmetric and Li/graphene-C/Li_3N||Li/graphene-C/Li_3N cells for different cycles at 1 mA cm^{-2} and 1 mAh cm^{-2}. As shown in Fig. 4a, the Li/graphene-C/Li_3N||Li/graphene-C/Li_3N symmetric cell exhibited stable cycling for over 1000 hours (Fig. 4a), delivering a stable overpotential of around 36 mV. In contrast, a much higher overpotential of ~340 mV was observed at the beginning of the first cycle for the Li||Li symmetric cell cycled under the same conditions, due to the high interfacial resistance of the passivation layer. Then the overpotential of the Li||Li symmetric cell decreased to ~48 mV after the first cycle, which was also consistent with the EIS result, indicating the break of the initial passivation layer and the inhomogeneous deposition of metallic Li with high surface area [48,49]. During cycling, the overpotential of the Li||Li symmetric cell continuously increased and it reached over 700 mV at the 500th cycle. To further investigate the rate capability of the Li/graphene-C/Li_3N electrode, the Li||Li symmetric cell and Li/graphene-C/Li_3N||Li/graphene-C/Li_3N symmetric cell were

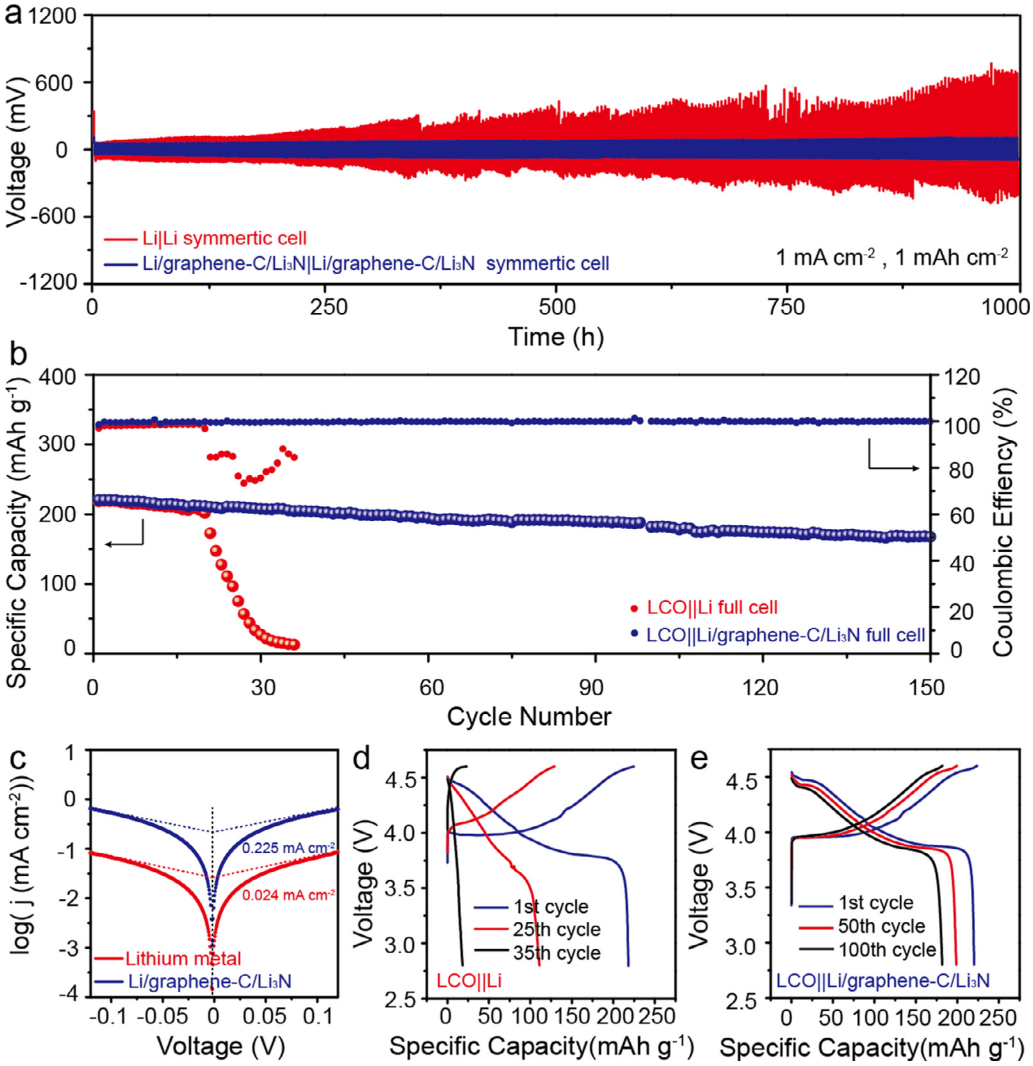

Fig. 4. Electrochemical performance of lithium metal electrode and Li/graphene-C/Li_3N electrode. (a) Lithium stripping/plating cycling of symmetric cells at 1 mA cm^{-2} and 1 mAh cm^{-2}. (b) Capacity *vs.* cycle number profiles of the LCO||Li and LCO||Li/graphene-C/Li_3N cells with high LCO capacity loading (~2.5 mAh cm^{-2}) and low areal capacity ratio of negative to positive electrodes (N/P ratio, 4). (c) Tafel profile obtained from cyclic voltammetry measurements after the first cycle at 1 mA cm^{-2} and 1 mAh cm^{-2}. (d, e) Voltage *vs.* capacity profiles of the LCO||Li (d) and LCO||Li/graphene-C/Li_3N (e) cells for various cycles.

also tested under the current density of 3 mA cm^{-2} with the fixed areal capacity of 1 mAh cm^{-2} (Fig. S11). The Li||Li symmetric cell showed a pretty high overpotential of 103 mV at the fifth cycle and it reached 172 mV after the 50th cycle. Short-cut occurred in the Li||Li symmetric cell at the 68th cycle (Fig. S12). In contrast, the Li/graphene-C/Li_3N||Li/graphene-C/Li_3N symmetric cell displayed a much lower overpotential of ~60 mV, and flat and smooth voltage curves for more than 300 cycles, suggesting that the introduction of high ion-conductive Li_3N interphase could enhance the lithium-ion transport, suppress side reactions and stabilize the structure (Fig. S12). Additionally, the Tafel profile showed that the exchange current density of the Li/graphene-C/Li_3N electrode (≈0.225 mA cm^{-2}) was higher than that of pure lithium metal electrode (≈0.024 mA cm^{-2}), which also supported the faster lithium ionic transport of Li/graphene-C/Li_3N electrode (Fig. 4c).

To further validate the superiorities of the Li/graphene-C/Li_3N electrode, high-voltage full cells were constructed by pairing with $LiCoO_2$ (LCO) cathode. Full cells with high cathode mass loading (~10.9 mg cm^{-2}) and low areal capacity ratio of negative to positive electrodes (N/P ratio, 4) were tested at 0.5 *C* (1 *C* = 220 mA g^{-1}) in the voltage range of 2.8 – 4.6 V. The LCO||Li/graphene-C/Li_3N full cell exhibited specific capacity of 220 mAh g^{-1}, and high areal capacity of 2.4 mAh cm^{-2}. The energy density reached as high as 694.05 Wh kg^{-1} based on the total mass of cathode and anode. Moreover, the cell showed stable cycling with a high reversible specific capacity of 168 mAh g^{-1} and capacity retention of 75.91% after 150 cycles. Although the LCO||Li full cell delivered a higher energy density of 722.8 Wh kg^{-1} at the first cycle, it quickly decayed after 20 cycles due to the quick decay of bare Li metal anode. (Fig. S13) Meanwhile, much smaller voltage hysteresis was observed for the LCO||Li/graphene-C/Li_3N full cell in comparison to the LCO||Li full cell during battery operation (Fig. 4d, e). For example, the average charge/discharge voltage of LCO||Li full cell is 4.066 V and 3.910 V respectively at the first cycle, and the voltage hysteresis is 0.156 V. Then with the further cycling, the voltage hysteresis of LCO||Li full cell increased to 0.916 V at the 40th cycle and which severely affected the battery cycling. In contrast, LCO||Li/graphene-C/Li_3N full cell showed a much smaller voltage hysteresis of 0.060 V at the first cycle and increased to 0.158 V at the 150th cycle at a slow rate of ~ 6 mV per cycle, indicating a less resistive and highly stable surface of Li/graphene-C/Li_3N electrode. (Fig. S14, S15) In addition, the Coulombic efficiency of LCO|| Li/graphene-C/Li_3N full cell was ~99.4% for more than 150 cycles. However, the LCO||Li full cell showed relatively lower Coulombic efficiency (< 98.0%) on cycling and declined sharply after 20 cycles.

3. Conclusions

In summary, to address the large volume change and unstable surface chemistry of metallic Li electrode, we demonstrated a Li/graphene-C/Li_3N electrode with graphene framework as host for metallic Li and ionically conductive Li_3N interphase to homogenize the Li^+ flux and suppress side reactions. The ionically conductive and electronically resistive surface Li_3N layer of the Li/graphene-C/Li_3N electrode was realized through the chemical reaction between molten lithium and the g-C_3N_4 layer on graphene/g-C_3N_4 composite film during their contact. Benefited from the synthetical effect of graphene framework and Li_3N protection surface layer, good electrochemical-mechanical stability of the electrode was realized. As a result, the Li/graphene-C/Li_3N electrode exhibited excellent electrochemical performance both in the symmetric cell and high-voltage full cell configurations. The LCO||Li/graphene-C/Li_3N full cell delivered a high energy density of 694.05 Wh kg^{-1} at potential range of 2.8 – 4.6 V and it showed high capacity retention of 75.91% for 150 cycles. These results provided a feasible design method for achieving stable lithium metal anode for rechargeable high energy density batteries.

Declaration of Competing Interest

The authors declare that they have no known competing financial interests or personal relationships that could have appeared to influence the work reported in this paper.

CRediT authorship contribution statement

Mintao Wan: Investigation, Data curation, Writing – original draft. **Xiangrui Duan:** Investigation, Data curation. **Hao Cui:** Investigation. **Junmou Du:** Data curation, Methodology. **Lin Fu:** Investigation, Methodology. **Zihe Chen:** Data curation. **Zhao Lu:** Investigation. **Guocheng Li:** Investigation. **Yuanjian Li:** Investigation. **Eryang Mao:** Investigation. **Li Wang:** Conceptualization, Methodology, Writing – review & editing. **Yongming Sun:** Supervision, Conceptualization, Methodology, Writing – review & editing.

Acknowledgments

Y. S. acknowledges the financial support by theNational Natural Science Foundation of China project (52072137) and the Innovation Fund of Wuhan National Laboratory for Optoelectronics of Huazhong University of Science and Technology. The authors would like to thank the Analytical and Testing Center of Huazhong University of Science and Technology as well as the Center for Nanoscale Characterization & Devices of Wuhan National Laboratory for Optoelectronics for providing the facilities to conduct the characterization.

Supplementary materials

Supplementary material associated with this article can be found, in the online version, at doi:10.1016/j.ensm.2022.01.044.

References

[1] S. Chu, A. Majumdar, Nature 488 (2012) 294–303.
[2] R. Van Noorden, Nature 507 (2014) 26–28.
[3] B. Dunn, H. Kamath, J.-M. Tarascon, Science 334 (2011) 928–935.
[4] M. Armand, J.M. Tarascon, Nature 451 (2008) 652.
[5] Y. Liang, C.-Z. Zhao, H. Yuan, Y. Chen, W. Zhang, J.-Q. Huang, D. Yu, Y. Liu, M.-M. Titirici, Y.-L. Chueh, H. Yu, Q. Zhang, Infomat 1 (2019) 6–32.
[6] B. Scrosati, J. Garche, J. Power Sources 195 (2010) 2419–2430.
[7] M.S. Whittingham, Chem. Rev. 114 (2014) 11414–11443.
[8] Y. Li, J. Wu, B. Zhang, W. Wang, G. Zhang, Z.W. Seh, N. Zhang, J. Sun, L. Huang, J. Jiang, J. Zhou, Y. Sun, Energy Storage Mater. 30 (2020) 250–259.
[9] J. Alvarado, M.A. Schroeder, M.H. Zhang, O. Borodin, E. Gobrogge, M. Olguin, M.S. Ding, M. Gobet, S. Greenbaum, Y.S. Meng, K. Xu, Mater. Today 21 (2018) 341–353.
[10] J. Liu, Z. Bao, Y. Cui, E.J. Dufek, J.B. Goodenough, P. Khalifah, Q. Li, B.Y. Liaw, P. Liu, A. Manthiram, Y.S. Meng, V.R. Subramanian, M.F. Toney, V.V. Viswanathan, M.S. Whittingham, J. Xiao, W. Xu, J. Yang, X.-Q. Yang, J.-G. Zhang, Nat. Energy (2019), doi:10.1038/s41560-019-0338-x.
[11] N. Imanishi, O. Yamamoto, Mater. Today Adv. (2019) 4.
[12] J. Lu, C. Zhan, T. Wu, J. Wen, Y. Lei, A.J. Kropf, H. Wu, D.J. Miller, J.W. Elam, Y.-K. Sun, X. Qiu, K. Amine, Nat. Commun. (2014) 5.
[13] Y.K. Sun, Z.H. Chen, H.J. Noh, D.J. Lee, H.G. Jung, Y. Ren, S. Wang, C.S. Yoon, S.T. Myung, K. Amine, Nat. Mater 11 (2012) 942–947.
[14] P. Yan, J. Zheng, M. Gu, J. Xiao, J.-G. Zhang, C.-M. Wang, Nat. Commun. (2017) 8.
[15] S. Chen, J. Zheng, D. Mei, K.S. Han, M.H. Engelhard, W. Zhao, W. Xu, J. Liu, J.-G. Zhang, Adv. Mater. (2018) 30.
[16] S. Li, W. Zhang, Q. Wu, L. Fan, X. Wang, X. Wang, Z. Shen, Y. He, Y. Lu, Angew. Chem.-Int. Edit. 59 (2020) 14935–14941.
[17] C. Yan, Y.-X. Yao, X. Chen, X.-B. Cheng, X.-Q. Zhang, J.-Q. Huang, Q. Zhang, Angew. Chem.-Int. Edit. 57 (2018) 14055–14059.
[18] J. Wang, Y. Yamada, K. Sodeyama, C.H. Chiang, Y. Tateyama, A. Yamada, Nat. Commun. (2016) 7.
[19] J. Lu, Z. Chen, F. Pan, Y. Cui, K. Amine, Electrochem. Energy Rev. (2018), doi:10.1007/s41918-018-0001-4.
[20] J.B. Goodenough, K.-S. Park, J. Am. Chem. Soc. 135 (2013) 1167–1176.
[21] P. Albertus, S. Babinec, S. Litzelman, A. Newman, Nat. Energy 3 (2018) 16–21.
[22] W. Xu, J. Wang, F. Ding, X. Chen, E. Nasybutin, Y. Zhang, J.-G. Zhang, Energy Environ. Sci. 7 (2014) 513–537.
[23] C.C. Fang, J.X. Li, M.H. Zhang, Y.H. Zhang, F. Yang, J.Z. Lee, M.H. Lee, J. Alvarado, M.A. Schroeder, Y.Y.C. Yang, B.Y. Lu, N. Williams, M. Ceja, L. Yang, M. Cai, J. Gu, K. Xu, X.F. Wang, Y.S. Meng, Nature 572 (2019) 511.
[24] I. Yoshimatsu, T. Hirai, J. Yamaki, J. Electrochem. Soc. 135 (1988) 2422–2427.
[25] C. Niu, D. Liu, J.A. Lochala, C.S. Anderson, X. Cao, M.E. Gross, W. Xu, J.-G. Zhang, M.S. Whittingham, J. Xiao, J. Liu, Nat. Energy (2021), doi:10.1038/s41560-021-00852-3.
[26] Q. Pang, X. Liang, A. Shyamsunder, L.F. Nazar, Joule 1 (2017) 871–886.
[27] L. Suo, Y.-S. Hu, H. Li, M. Armand, L. Chen, Nat. Commun. 4 (2013).
[28] Q. Pang, A. Shyamsunder, B. Narayanan, C.Y. Kwok, L.A. Curtiss, L.F. Nazar, Nat. Energy (2018), doi:10.1038/s41560-018-0214-0.
[29] C. Yang, K. Fu, Y. Zhang, E. Hitz, L. Hu, Adv. Mater. (2017) 29.
[30] M.S. Kim, J.-H. Ryu, Y.R. Deepika, I.W. Lim, K.-R. Nah, L.A. Lee, Archer and W. Il Cho, *Nat. Energy* (2018), doi:10.1038/s41560-018-0237-6.
[31] Z. Tu, S. Choudhury, M.J. Zachman, S. Wei, K. Zhang, L.F. Kourkoutis, L.A. Archer, Nat. Energy (2018), doi:10.1038/s41560-018-0096-1.
[32] X. Liang, Q. Pang, I.R. Kochetkov, M.S. Sempere, H. Huang, X.Q. Sun, L.F. Nazar, Nat. Energy 2 (2017) 7.
[33] M.T. Wan, S.J. Kang, L. Wang, H.W. Lee, G.W. Zheng, Y. Cui, Y.M. Sun, Nat. Commun. 11 (2020) 10.
[34] R. Zhang, N.-W. Li, X.-B. Cheng, Y.-X. Yin, Q. Zhang, Y.-G. Guo, Adv. Sci. (Weinheim, Baden-Wurttemberg, Germany) 4 (2017) 1600445.
[35] C. Niu, H. Pan, W. Xu, J. Xiao, J.-G. Zhang, L. Luo, C. Wang, D. Mei, J. Meng, X. Wang, Z. Liu, L. Mai, J. Liu, Nat. Nanotechnol. 14 (2019) 594–601.
[36] C.-P. Yang, Y.-X. Yin, S.-F. Zhang, N.-W. Li, Y.-G. Guo, Nat. Commun. 6 (2015) 8058.
[37] C. Yang, Y. Yao, S. He, H. Xie, E. Hitz, L. Hu, Adv. Mater. (2017) 29.
[38] J. Duan, Y. Zheng, W. Luo, W. Wu, T. Wang, Y. Xie, S. Li, J. Li, Y. Huang, Natl. Sci. Rev. 7 (2020) 1208–1217.
[39] W.-J. Ong, L.-L. Tan, Y.H. Ng, S.-T. Yong, S.-P. Chai, Chem. Rev. 116 (2016) 7159–7329.
[40] D. Lin, Y. Liu, Z. Liang, H.-W. Lee, J. Sun, H. Wang, K. Yan, J. Xie, Y. Cui, Nat. Nanotechnol. 11 (2016) 626.
[41] Y. Guo, P. Niu, Y. Liu, Y. Ouyang, D. Li, T. Zhai, H. Li, Y. Cui, Adv. Mater. (2019) 31.
[42] L. Fu, X. Wang, L. Wang, M. Wan, Y. Li, Z. Cai, Y. Tan, G. Li, R. Zhan, Z.W. Seh, Y. Sun, Adv. Funct. Mater. (2021), doi:10.1002/adfm.202010602.
[43] S. Ye, L. Wang, F. Liu, P. Shi, H. Wang, X. Wu, Y. Yu, Adv. Energy Mater. (2020) 10.
[44] Y. Li, Y. Sun, A. Pei, K. Chen, A. Vailionis, Y. Li, G. Zheng, J. Sun, Y. Cui, ACS Central Sci. 4 (2018) 97–104.
[45] N. Piao, X. Ji, H. Xu, X. Fan, L. Chen, S. Liu, M.N. Garaga, S.G. Greenbaum, L. Wang, C. Wang, X. He, Adv. Energy Mater. 10 (2020) 1903568.
[46] X.-Q. Zhang, X. Chen, L.-P. Hou, B.-Q. Li, X.-B. Cheng, J.-Q. Huang, Q. Zhang, Acs Energy Lett. 4 (2019) 411–416.
[47] J. Liu, R. Jiang, X. Wang, T. Huang, A. Yu, J. Power Sources 194 (2009) 536–540.
[48] L. Fan, H.L. Zhuang, W. Zhang, Y. Fu, Z. Liao, Y. Lu, Adv. Energy Mater. (2018) DOI: 10.1002/aenm.201703360, 1703360-n/a.
[49] S.-S. Chi, Y. Liu, W.-L. Song, L.-Z. Fan, Q. Zhang, Adv. Funct. Mater. (2017) 27.